Combustion Synthesis and Spark Plasma Sintering of Apatite-Tricalcium phosphate Nanocomposites

Damiano Angioni[1], Roberto Orrù[1,*], Giacomo Cao[1],
Sebastiano Garroni[2], Pier Carlo Ricci[3], Khachatur V. Manukyan[4]

[1]*Dipartimento di Ingegneria Meccanica, Chimica, e dei Materiali, Unità di Ricerca del Consorzio Interuniversitario Nazionale per la Scienza e Tecnologia dei Materiali (INSTM), Università degli Studi di Cagliari, 09123, Cagliari, Italy*

[2]*Dipartimento di Scienze Chimiche, Fisiche, Matematiche e Naturali, Università degli Studi di Sassari, 07100, Sassari, Italy*

[3]*Dipartimento di Fisica, Università degli Studi di Cagliari, 09042, Monserrato, Cagliari, Italy*

[4]*Department of Physics and Astronomy, University of Notre Dame, Notre Dame, 46556, IN, United States*

Corresponding author: Roberto Orrù (roberto.orru@unica.it)

Abstract

Nanostructured biphasic calcium phosphates were produced in this work by spark-plasma sintering (SPS) of precursor powders prepared by solution combustion synthesis (SCS). The apatite phase content in the product obtained by SCS was maximized using a fuel to oxidizer ratio of 1.1. After a post-synthesis air-annealing step conducted a 700°C/3h, powders consisted of 83 wt.% of carbonated apatite, with average crystallite size less than 70 nm, and β- and α-TCP (tricalcium phosphate), as secondary phases. Detailed structural analyses evidenced that the original nanostructure was retained after sintering at 900°C, with the obtainment of nearly

91 % dense, apatite-rich, biphasic bioceramics, with grains size of about 100 nm. The developed nanostructured biphasic material is expected to possess a higher resorption rate than standard microcrystalline hydroxyapatite, which makes it preferable for bone tissue regeneration.

Keywords

Nanocomposites, Hydroxyapatite; Tricalcium phosphate; Solution Combustion; Spark Plasma Sintering (SPS)

https://doi.org/10.1016/j.ceramint.2023.05.219

1. Introduction

Due to their biocompatibility, compositional and structural similarity to the inorganic phase of hard tissues, synthetic calcium orthophosphates have attracted a strong interest during the past 50 years for biomedical applications **[1]**. In this context, stoichiometric hydroxyapatite ($Ca_{10}(PO_4)_6(OH)_2$), also referred to as HA or HAp, is the most representative, investigated, and generally employed bioactive ceramic to date. The main concern related to HA is its low solubility, i.e., about 0.0003 g/L at 25°C **[1]**, which makes it biologically stable once introduced into the human body. The latter aspect is not desirable in modern regenerative medicine, where biomaterials capable to be progressively resorbed are searched for. On the other hand, tricalcium phosphates ($Ca_3(PO_4)_2$ or TCP), which can be formed in two phases (β-TCP and α-TCP), have acquired significant importance due to their superior biodegradability, compared to that of HA, associated with their relatively higher dissolution **[1]**. Nonetheless, dissolution should not occur too fast for bone bonding. In this framework, the combination of HA with TCP to generate biphasic composites with suitable resorption rates under the physiological conditions, in between those of individual phases, was explored **[2]**.

The characteristics of these bioceramics depend on their preparation routes. Several methods have been proposed to prepare HA-β-TCP biphasic calcium phosphates (BCP). The latter can be produced after heat treatment, above certain temperatures, of other calcium phosphates **[3-8]**, precipitation method **[9-12]**, Pechini based liquid-mix technique **[13]**, microwave irradiation **[14]**, sol-gel **[15]**, combined wet mechano-chemical - solid-state synthesis **[16]**, and solution combustion **[17-20]**.

In this regard, preparation methods capable to provide synthesis products in the form of nanopowders are quite useful to mimic better not only the composition, but also the size of the mineral constituent of hard tissues, i.e., the biological apatite, which is nanocrystalline **[21]**.

Along this line, solution combustion synthesis (SCS) represents a rapid and simple technique for the preparation of a wide variety of nanoscale materials **[19]**. Accordingly, several investigations have been addressed to the synthesis of calcium phosphate-based bioceramic powders by SCS **[19-20]**. Such studies differ from each other in the type of fuel used (glycine, urea, citric acid), heating source (furnace, hot plate, microwave), doping elements (Cr, Al, Sr, Eu), and for the characterization of the combustion synthesized products **[20]**. In addition, most of these works focused on the synthesis and characterization of powders. To the best of our knowledge, only two investigations also considered sintering of combustion products **[22-23]**. Specifically, the processing route reported by **Canillas et al. [22]**, to produce samples consisting of HA (main) and β-TCP (minor) phases, was based on the following four stages: 1) SCS (fuel: urea, Calcium source: $Ca(NO_3)_2{\cdot}4H_2O$, phosphate source: $(NH_4)_2HPO_4$, additive: HNO_3); 2) 8h duration milling treatment, for breaking the formed agglomerates; 3) uniaxial pressing at 200MPa of the obtained powders; 4) pressureless sintering for 2 h at 1230°C. The obtained samples show low residual porosities, i.e., < 6% (aqueous HA) and < 2% (HNO_3 HA). Similarly, the preparation of HA products carried out by **Ghosh et al. [23]** involved the following processing steps: 1) SCS (fuel: citric acid, Calcium source: $Ca(NO_3)_2{\cdot}4H_2O$, phosphate source: $(NH_4)_2HPO_4$, additive: HNO_3); 2) powder calcination up to 1300°C; 3) cold pressing of calcinated powder in the presence of 6% polyvinyl alcohol; 4) pressureless sintering at 1200 and 1250°C.

Although both studies evidenced the importance of the preparation of small grains size of apatite, similar to that present in natural bone tissues, such information was not reported for the sintered samples. However, it is expected that the adopted sintering temperatures (equal to or above 1200°C) during step 4) are too severe to retain the original grains size of apatite at the nanoscale. To avoid or limit grain growth during powder consolidation, the process needs to be apparently conducted

under milder temperatures and shorter processing times, with respect to those ones reported by **Canillas et al. [22]** and **Ghosh et al. [23]**. Due to the more convenient operating conditions generally required compared to conventional techniques, the use of the efficient Spark Plasma Sintering (SPS) technology was exploited in the literature for the obtainment of bulk nanostructured calcium phosphates (apatites and/or TCP) from powder prepared by precipitation **[24-29]** or hydrothermal **[25,30-31]** methods. The characteristics of the resulting SPS products depended on the operating conditions and the starting powders produced by the latter synthesis techniques, i.e., fine grained **[24-27,29-30]** or amorphous **[28-29]**. Sintering temperatures equal to or exceeding 900°C generally led to dense samples with grain size above 200 nm **[26,30-31]**. In contrast, nanostructured products with a relative density below 80% are usually obtained when operating at lower temperatures **[26-29]**. As an exception, **Eriksson et al. [31]** were able to fabricate highly dense apatite products with an average grain size of about 85 nm, taking advantage of high-pressure cells, which allowed them the application of mechanical pressures up to 500 MPa during SPS.

The present work is aimed to produce bulk nanostructured apatite-based bioceramics by combining the SCS method with SPS for the first time. Specifically, the influence of the fuel to oxidizer ratio (ϕ) on the synthesis reaction ignition and product composition will be first systematically studied. Then, the effect of the annealing temperature on the compositional and microstructural characteristics of the resulting powders will be analyzed in detail to minimize the presence of secondary phases. Finally, bulk nanostructured biphasic HA-TCP samples will be produced under optimal SPS conditions.

2. Materials and methods

2.1 Powders synthesis

The procedure for the SCS of apatite, shown in Supplementary **Figure S1**, was adapted from that proposed by **Ghosh et al. [32]**. Aqueous solutions of calcium nitrate tetrahydrate ($Ca(NO_3)_2$ $4H_2O$ >99.0%, Sigma-Aldrich, Italy) and diammonium phosphate ($(NH_4)_2HPO_4$ >99.0%, Sigma-Aldrich, Italy) were prepared to obtain concentrations equal to 2.72M and 2.09M, respectively. Subsequently, such solutions were mixed in proper amounts to satisfy the stoichiometry of the following base reaction:

$$10\ \mathrm{Ca(NO_3)_2 \cdot 4\ H_2O} + 6\ \mathrm{(NH_4)_2HPO_4} + \Phi\ \frac{100}{9}\ \mathrm{NH_2CH_2COOH} + 9\mathrm{O_2} \rightarrow$$
$$\rightarrow \mathrm{Ca_{10}(PO_4)_6(OH)_2} + \frac{194}{9}\ \mathrm{N_2} + \frac{200}{99}\ \mathrm{CO_2} + \frac{844}{9}\ \mathrm{H_2O} \qquad (1)$$

The solution was kept under continuous stirring until a white precipitate is formed. A 14M nitric acid solution (70% HNO_3 >99.99%, Sigma-Aldrich, Italy) was then added dropwise to adjust the pH value to 1, and the resulting clear solution was stirred for 15 min. The fuel, glycine (NH_2CH_2COOH ReagentPlus >99%, Sigma-Aldrich, Italy), was then introduced to the solution in suitable quantities depending on the value of the ϕ parameter (varied in the range 0.7 to 1.4), according to Eq. 1 **[32]**. After an additional 15 min of stirring, the dehydration phase started. The solution temperature was held between 70 and 80°C for 20 min, using a heating plate (TK22, Kartell, Italy). The plate temperature was then increased to 370°C until the SCS reaction occurred.

The resulting powders were then grounded in an agate mortar and, subsequently, heat treated in a muffle furnace (LT 24/11/B410, Nabertherm, Lilienthal, Germany), at temperatures ranging from 600 to 900°C, to remove/reduce undesired secondary phases. Annealing consisted of heating powders for 3 h at the holding temperature,

which was reached at a rate of 5°C/min, followed by a natural cooling step. To guarantee the reproducibility of the process, each test was replicated at least twice.

2.2 Bulk samples

Powder consolidation was carried out using the SPS equipment 515S model (Fuji Electronic Industrial Co., Ltd., Kanagawa, Japan), which was properly evacuated down to about 20 Pa before electric current application. This apparatus was set to operate with a current sequence of 12 ON pulses followed by 2 OFF pulses, and 3.3 ms as characteristic time of single pulse. About 1.6 g of the heat-treated powder was placed inside a graphite die cylinder (35 mm external diameter, 15 mm inside diameter, 40 mm height) between two plungers (14.7 mm diameter, 30 mm height), consisting of AT101 graphite (ATAL Srl., Italy). The die was covered with a 3 mm thick graphite felt (Atal s.r.l., Italy) to reduce heat losses during the SPS process. The temperature was measured using a K-type thermocouple (TC Misure e Controlli S.R.L., Italy) inserted in a small hole drilled on the external surface of graphite dies, placed 1-2 mm far from the sample. A graphite foil (0.13 mm thickness, Alfa Aesar, Karlsruhe, Germany) was introduced between the powders and the inner walls of die/plungers to facilitate sample release after sintering.

The temperature was firstly increased at a rate of 50°C/min from the room value to a level, 100°C below the maximum (T_D). To limit possible overshooting problems, the final T_D value was then reached at the lower rate of 10°C/min. The 5 min isothermal heating at T_D was followed by temperature decrease at a rate of 50°C/min down to 300°C, followed by a natural cooling step. The applied pressure (P) was raised to 70 MPa in about 1 min, then maintained constant during both non-isothermal and isothermal heating steps, and finally gradually reduced during sample cooling.

Various bulk samples were produced at different T_D (750-900°C). Consolidated samples were carefully polished using abrasive paper to remove residual impurities

from the graphite parts, to provide final cylindrical disks of about 14.7 mm diameter and 2.5-3 mm height. Each experimental condition was replicated at least twice.

2.3 Characterization

The composition and microstructure of both the powders and bulk samples were first assessed by X-Ray Diffraction (XRD) analysis (Philips PW 1830, Netherlands) using a Cu Kα radiation, under the following experimental conditions: Range: 10-130°; Step: 0.05°; dwell time: 10 sec. Phases, their amount (wt.%), and the related structural parameters were estimated according to the Rietveld method using the MAUD program **[33]**.

In addition, Raman spectroscopy measurements were carried out using an MS750 spectrograph (sol-instruments, Minsk, Belarus) equipped with 1200-600 gr/mm grating. The laser beam (785 nm), with a power of about 7.5 mW, was focalized by Olympus objectives (50x and 100x). Measurements were performed at room temperature, with a spectral resolution of 1 cm^{-1}. At least ten acquisitions were taken in different parts of each examined sample, resulting from an average of three measures of 120 s.

Furthermore, detailed scanning electron microscopy (SEM) and transmission electron microscopy (TEM) analyses were conducted to investigate the composition, morphology, and atomic structure of powders and consolidated samples.

Specifically, a Helios Nanolab 600 instrument (Thermo Fisher Scientific), equipped with a dual electron/ion beam system was used to acquire secondary-electron SEM images and for the preparation of ~70 nm thin slices for cross-sectional TEM measurements. Before microscopy measurements, all samples were coated with an iridium layer (2.5 nm thick). Grains size distribution in bulk samples was evaluated from SEM micrographs using the ImageJ software **[34]**.

Thin slices were prepared for the TEM analysis from bulk samples. A 1 μm thick platinum layer was deposited onto a selected rectangular area of 10 μm × 0.5 μm. Approximately 5 μm deep trenches (with a 52◦ base angle) were milled by a gallium beam on both sides of the platinum layer (accelerating voltage: 5 keV, milling current: 27 nA). Then, the slice was lifted from the sample and polished to about 70 nm thickness under an accelerating voltage of 5 keV and a milling current of 700 pA. In this way, a clean cross-section of the samples for TEM images was produced without milling artifacts.

A Titan 300 TEM equipment (FEI, USA, with a resolution of 0.136 nm in scanning mode, information limit: ~0.1 nm at high-resolution mode) was used to examine the synthesized powders. About 0.1 g of the material was sonicated in 10 ml of deionized water for 10 minutes, few drops of it were placed onto a 300 mash Cu TEM grid with lacey carbon films and naturally dried overnight. A cleaning procedure in 20%O_2-Ar plasma was performed for 1 minute prior to measurements.

Spectra 300 (Thermo Fisher Scientific) TEM microscope (resolution: 50 pm at 300 kV in scanning TEM mode) equipped with GIF Continuum K3 camera (Gatan, to perform low-dose high-resolution imaging in beam-sensitive samples) was used for the TEM analyses of the thin slices lifted from the consolidated samples. EDS analysis was carried out by a silicone drift detector (Thermo Fisher) with energy resolution of ~ 25 eV at 5.9 keV.

TEM images were then processed by the ImageJ software **[34]**, while TEM-derived diffraction patterns were examined by the ProcessDiffraction software **[35-36]**. Finally, all the d-spacing assignments are based on the calculations made by the software VESTA **[37]**.

The density of the bulk samples was measured by the Archimedes' method using ethanol as immersing medium and an Ohaus Explorer Pro (Ohaus Corporation, NJ, USA) analytical balance (± 0.0005 g precision) to weight them. Relative densities were

calculated by considering as a reference value the theoretical density of stoichiometric HA (3.16 g/cm^3).

3 Results and discussion

3.1 Solution combustion synthesis

The effect of an increase of the ϕ value on the ignition time of the SCS reaction (1) is shown in **Figure S2**. Reaction ignition did not occur at ϕ ratio below 0.7 or above 1.4. Moreover, the condition under which the reaction ignition was observed to occur earlier is ϕ = 1 (stoichiometric mixture), whereas it took a longer time for lower or higher values of this parameter.

3.1.1 XRD analysis

The XRD patterns of the synthesized products obtained for different ϕ ratios are compared in **Figure 1**. Apatite is always the main phase present in the synthesis products, regardless of the specific ϕ value considered. The relative intensities of the apatite peaks at 32.34 and 33.08 deg are coherent with the ones of A-type substitution in Carbonated apatite ($Ca_{10}(PO_4)_6(OH)_{2-2x}(CO_3)_x$) phases. Indeed, while peak intensity at 33.08 deg in stoichiometric apatite is relatively higher than that at 32.34 deg, the opposite occurs in carbonated apatite **[38]**.

Apart from apatite, some secondary phases are also present in the synthesized powders, namely TCP (in both α and β forms), $CaCO_3$, $CaHPO_4$, and small amounts of CaO. Due to XRD patterns complexity and broad peaks associated with the nanostructured nature of the synthesized powders, the general trend for the content of secondary phases is not easy to obtain. Nonetheless, it is possible to state that lower amounts of $CaHPO_4$ and $CaCO_3$ are achieved when ϕ is in the range of 1.0-1.2. In addition, XRD peaks intensity of the TCP phase are minimized when operating at ϕ

= 1.1. Therefore, powders obtained at ϕ = 1.1, which displayed the most desirable composition, were further analysed by Rietveld refinement to quantitatively estimate phases amount. The obtained results are reported in **Figure S3a** and **Table S1**. The phases identified by this analysis and their relative amounts (wt.%) are: apatite (47.4), $Ca(HPO_4)$ (20.8), β-TCP (11.9), $CaCO_3 \cdot 6(H_2O)$ (9.6), α-TCP (6.4), $CaCO_3$ (3.7), and CaO (0.2). The presence of possible additional minor phases is not excluded. Furthermore, the estimation provided by Rietveld analysis for crystallite average size of apatite in SCS powder is approximately 65 nm (**Table S1**).

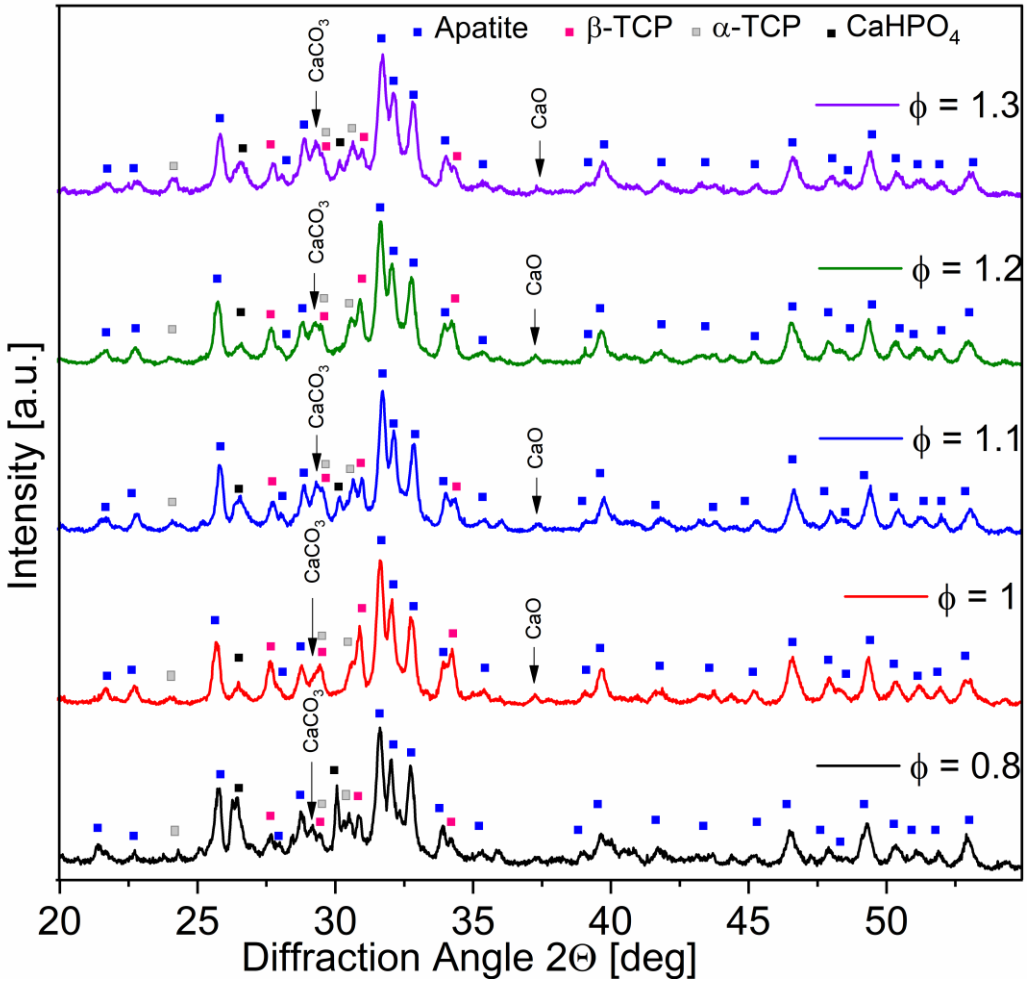

Figure 1. Effect of the fuel to oxidizer ratio (ϕ) on the composition of the SCS products.

The SCS products obtained for ϕ= 1.1 were annealed at 600-900 °C. The XRD patterns for samples annealed at 600 and 700°C are shown in **Figure S3b** and **Figure S3c**,

respectively. Structural parameters and the amount of each phase for all annealed samples are also reported in supplementary **Table S1**. Phases content (wt.%) as well as crystallites size of apatite and β-TCP are plotted in **Figure S4a** and **S4b**, respectively, as a function of the annealing temperature.

It is found that the larger relative amount of apatite in the product is obtained when the SCSed powders are annealed at 700°C. On the other hand, an increase of the temperature to 800°C or higher values produces the partial transformation of apatite to β-TCP. A marked crystallite growth is also observed when the heat treatment temperature exceeded 700°C (**Figure S4b**).

3.1.2 Raman spectroscopy

Powder samples synthesized with ϕ = 1.1 before and after their annealing at different temperature have also been examined by Raman spectroscopy. **Figure 2** indicates that the 960 cm^{-1} peak (ν_1-PO4, main one of apatite) is the most intense in all spectra, supporting the fact that apatite is the main phase present in the as-synthesized powders and annealed products, regardless of the heat-treatment conditions. In addition, as evidenced in **Figure S5**, the FWHM of such peak decreases when increasing the annealing temperature, suggesting that crystallites growth takes place. Furthermore, β-TCP peaks are clearly seen in spectra corresponding to samples heat treated at 800 and 900°C. This finding is evidenced in more detail in **Figure S6,** where it is seen that the signal of β-TCP significantly increases when the annealing temperature is augmented from 700 to 800°C. This outcome is consistent with the Rietveld analysis results shown in **Figure S3a** and **Table S1** and can be readily due to the partial apatite decomposition into β-TCP as the annealing temperature overcomes 700°C.

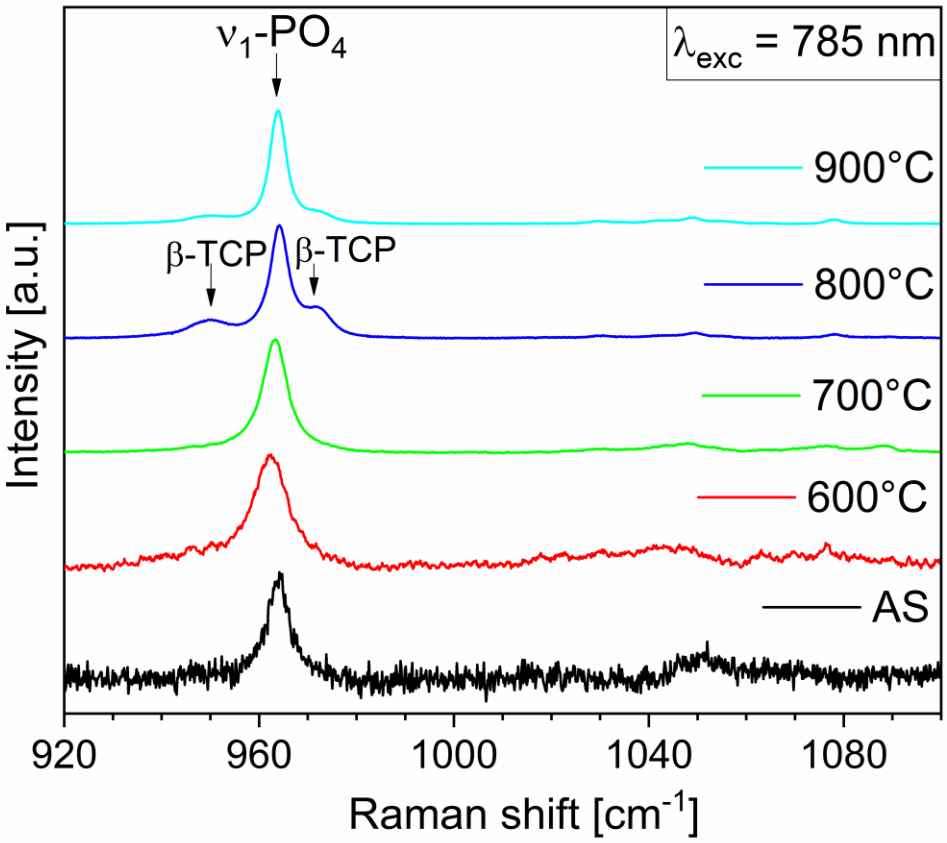

Figure 2. Raman spectra of combustion products (ϕ=1.1) before and after being annealed at different temperatures.

Figure S6 shows also that the intensity of the peak associated with the v1 mode of CO_3 group in calcium carbonate (1086 cm^{-1}) decreases as the annealing temperature is increased. This is consistent with the $CaCO_3$ dissociation temperature of approximately 800°C **[39]**. It should be noted that $CaCO_3$ was not revealed in samples annealed at 700°C, likely because its content is below the detection limit of XRD analysis.

Another important information provided by the Raman spectra (**Figure S6)** is related to the bands analyzed to estimate the carbonation level of apatite. Following **Awonusi et al. [40]**, a fitting procedure was carried out to calculate the area of the 1075 cm^{-1} peak (ν_3-PO_4) with respect to the 960 cm^{-1} one. The resulting residual

carbonation level for the sample annealed at 700 °C was approximately 2 wt.%., while this amount tends to vanish for samples annealed at higher temperatures. It should be underlined that such carbonation data refer only to B-type substitution, since the previously cited fitting procedure involves ν_3-PO_4 bands only.

3.1.3 SEM and TEM analyses

SEM images relative to the combustion product (ϕ=1.1) prior and after being annealed at 700°C are reported in **Figure 3a** and **Figure 3b**, respectively. From these micrographs, it can be clearly seen that the heat treatment provided powders with more defined nanosized grains (**Figure 3b**) compared to the as-synthesized ones (**Figure 3a**). This result holds also true for the case of ϕ = 1 (not shown) and is likely a consequence of the removal of the amorphous material during annealing, as discussed afterwards.

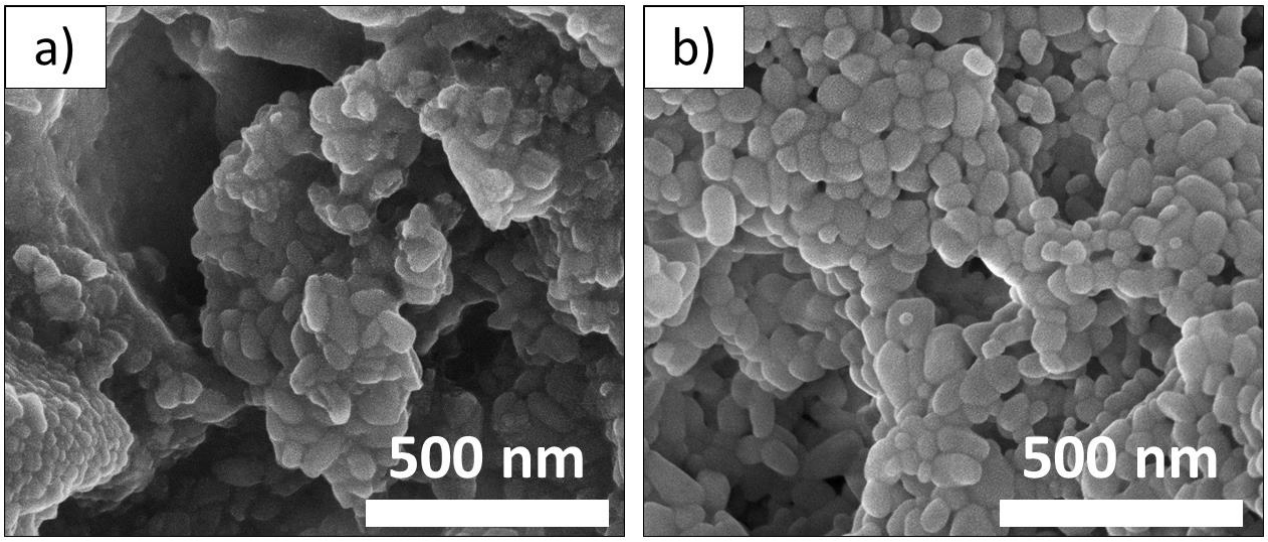

Figure 3. SEM micrographs of SCSed powders (ϕ=1.1) before (a) and after (b) being heat treated at 700°C.

Untreated and annealed powders have been also examined by TEM. It should be noted that stoichiometric compounds (i.e., HA, TCP, etc.) were used as literature data reference for TEM analysis, i.e., all the d-spacing and angles related to each lattice corresponded to stoichiometric formulations, instead of the non-stoichiometric phases possibly formed during SCS.

As for the as-synthesized powders, TEM observations evidenced the presence of two distinct morphological features, indicated hereto after as M1 and M2.

A bright-field image of a representative particle with M1-type morphology is shown in **Figure 4a** along with the corresponding SADP results. It is seen that the obtained diffraction pattern corresponds to an amorphous structure. However, **Figure S7**, resulting from longer exposure to the electron beam of the same spatial region, also evidenced some diffraction spots present at different positions. This is assumed to be the result of the occurrence of the partial transition of the amorphous phase to a crystalline one, apparently induced by the electron beam. The distance between such diffraction spots was then converted into d-spacing in the direct lattice. The obtained values, indicated in the same figure, are compared to those of HA. The resulting 2.3/2.5 Å values are rather close to (2, 2, 0) and (3, 0, 1) planes' d-spacing (2.35 and 2.52 Å respectively), while 1.68/1.72 Å values are similar to (0, 0, 4) and (1, 0, 4) planes' d-spacing (1.682 and 1.719 Å respectively).

A bright-field image of the M2-type morphology and the related diffraction analysis results are reported in **Figure 4b**. It is clearly evidenced the crystalline nature of such structure. The corresponding diffraction pattern relative to a particle of about 1 μm is also shown in **Figure 4b**, while the diffraction distribution is represented in terms of the scattering vector by the red line on the right side. The latter figure also reports the nominal position (vertical lines and relative Miller indices) of scattering vectors of stoichiometric HA and some of β-TCP. The thickness of the vertical lines is proportional to the nominal intensity of the indicated planes' signal. From this figure,

it is apparent that the diffraction peaks are well described by the HA structure, with minor amounts of β-TCP. On the other hand, the comparison with nominal values of other possible phases (α -TCP, $CaCO_3$, etc.) did not result in any match.

To provide additional information, high resolution-TEM (HR-TEM) imaging are also provided in **Figure S8**. The angle between ***m*** and ***n*** directions is 92°. The d-spacing of 2.73 Å, measured by the TEM image above, could be assigned to the (3, 0, 0) planes of the apatite structure (nominal value 2.72 Å), while the d-spacing of 1.72 Å could be ascribed to the (0, 0, 4) planes of the same structure (nominal value of 1.72 Å). The calculation of the angle between the previously cited directions (using the scalar product) is 90° (as quite evident from the h,k,l indexes), which is compatible with the measured value of about 91°.

The distance between the atoms across the ***q*** and ***r*** directions is 3.12 Å. Furthermore, the measured angle between the ***r*** and ***q*** directions is approximately 57°. Stoichiometric apatite (1, 2, 0) and (2, 1, 0) planes, with nominal d-spacing of 3.09 Å for both, enclose an angle of 60°.

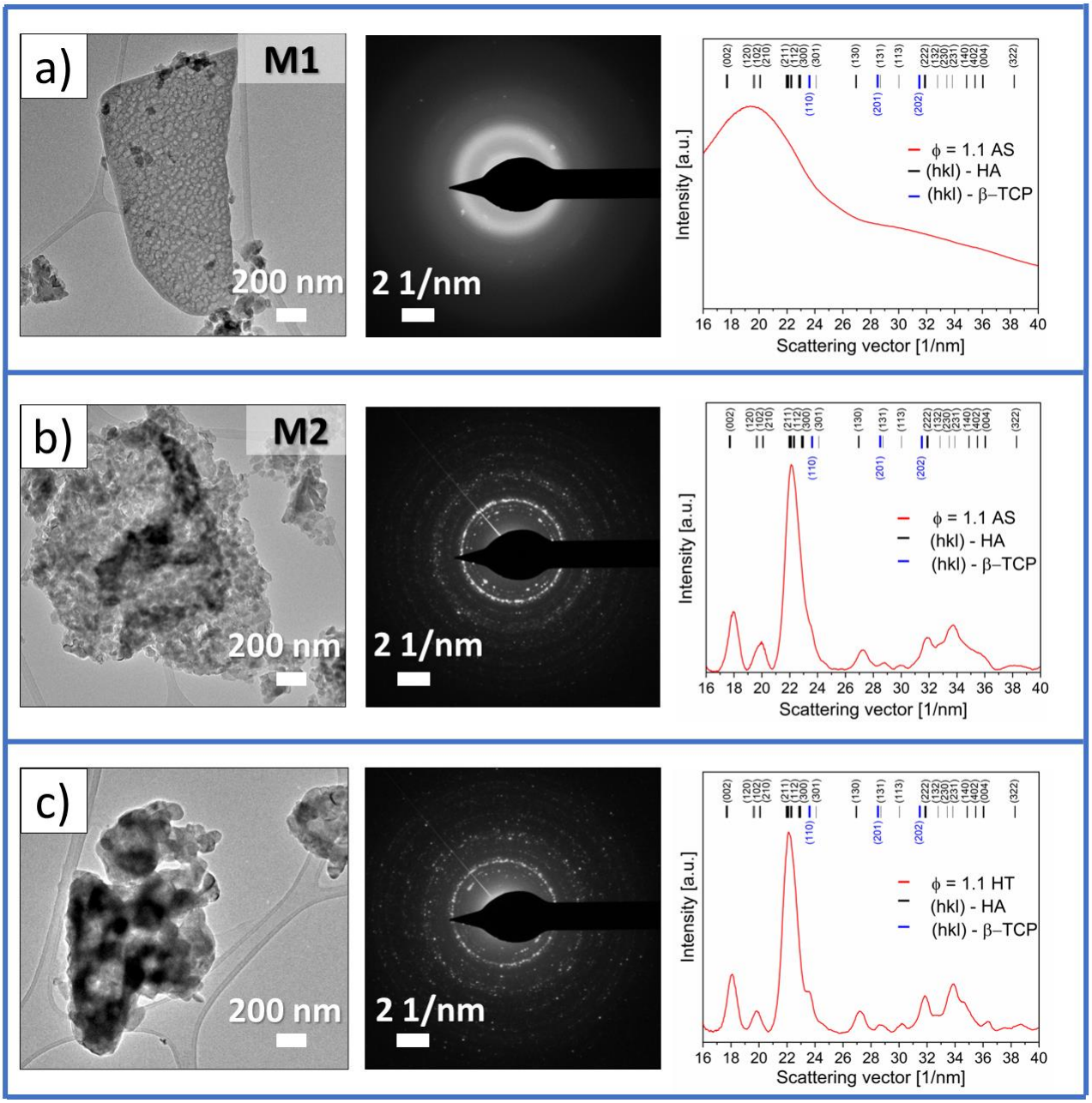

Figure 4. Bright field images of powders (ϕ=1.1), the related electron diffraction patterns, and diffraction intensities as a function of the scattering vector: (a) as synthesized powders, M1-type morphology; (b) as synthesized powders, M2-type morphology; (c) powders after being heat treated at 700°C.

The presence of the amorphous material was not detected after powder treatment.

TEM imaging and electron diffraction pattern for the sample annealed at 700°C are reported in **Figure 4c**. Bright-field image refers to porous particles of about 1-2 µm. The diffraction distribution is also shown in terms of scattering vector (red line) along with the nominal position (vertical lines and relative Miller indices) of scattering vectors of stoichiometric HA and β-TCP. The distribution profile for the diffraction pattern is generally well described by the HA structure, with a minor presence of β-TCP phase. This finding agrees with Rietveld analysis outcomes (**Table S1**).

The results obtained by the TEM imaging analysis are reported in **Figure S9**. The d-spacing of 3.24 Å and 3.08 Å could be ascribed to the (1, 0,2) and (2, 1, 0) planes of the apatite structure (nominal value for HA equal to 3.17 Å and 3.09 Å, respectively). It should be noted that the calculation of the angle between the previously cited directions is of about 61°, which is compatible with the measured value of approximately 59°.

Moreover, the d-spacing of 2.67 Å and 2.87 Å determined from TEM images could be related to the (1, 1, 0) and (1, 0, 2) planes of the β-TCP structure (nominal values of 2.68 Å and 2.95 Å, respectively). Also in this case, the calculation of the angle between the latter directions provided a value of 87°, very close to that one measured (approximately 86°).

To conclude, TEM data confirmed the presence of both crystalline apatite and β-TCP structures in heat-treated samples, in agreement with Rietveld refinement of XRD patterns.

3.2 Powder consolidation and bulk products characterization

3.2.1 XRD and Raman analyses

The combustion products annealed at 700°C were processed by SPS to obtain bulk samples. The XRD patterns of samples sintered at different temperature conditions are shown in **Figure S10**. The detected phases, their content, and the associated microstructural parameters determined according to the Rietveld refinement can be found in **Table S2**. To better evidence the effect produced by an increase of the sintering temperature on phases' amount and crystallite size, the related data are plotted in **Figure S11a and S11b**, respectively.

Figure S11a indicates that the relative amount of apatite decreases (from 83.0 to 76.2%) after the SPS process at 750°C, whereas that of β-TCP correspondingly increases (from 13.5 to 21.9%). This finding is a consequence of two events, i.e., the partial decomposition of apatite to generate β-TCP, and the transformation of α-TCP (which decreases from 3.2 to 1.8%, before and after SPS, respectively) to the β-counterpart. When the temperature was further raised, little changes in the apatite content were observed, while α-TCP was progressively reduced to 0.3% (850 °C) and disappeared at 900°C, which determined a slight increase of the β-TCP phase.

As for apatite crystallite size (**Figure S11b**), a moderate growth (from the initial 67 nm to 76 and 78 nm) occurred during SPS at T_D=750 and 850°C, respectively. In contrast, when the sintering temperature was 900°C, apatite crystallites grew to about 110 nm.

Data shown in **Table 1** indicate that an increase of the sintering temperature resulted in a marked powder densification improvement, with nearly 91% dense samples produced at T_D=900°C.

Table 1. Density of SPS samples at different dwell temperatures.

T_D [°C]	Density [g/cm^3]	Relative density [%]
750	1.87 ± 0.09	59.2 ± 2.8
850	2.62± 0.01	82.8 ± 0.2
900	2.86± 0.02	90.5 ± 0.6

Regardless of the dwell temperature conditions, it should be noted that the intensity of the peak at 33.08 deg is relatively higher than that at 32.34 deg (**Figure S10**), which is the opposite situation encountered with the starting powders (**Figure S3**). This outcome indicates that apatite decarbonation likely occurs during SPS. This feature will be investigated in detail in what follows.

Raman spectroscopy measurements carried out on the three differently sintered samples **(Figure S12)**, evidenced that the 960 cm^{-1} vibration peak (ν_1-PO_4,) is always the most intense, thus further supporting the fact that apatite is the primary phase present, regardless of the SPS conditions. In addition, β-TCP bands indicate that an increase in this phase occurred after SPS, which is also consistent with the results arising from the Rietveld analysis.

Awonusi et al. [40] procedure evidenced that no residual B-type CO_3^{2-} is present in SPS samples, to confirm that apatite decarbonation took place during the sintering process. In this regard, an important role is likely played by the environmental conditions (vacuum) adopted to perform SPS experiments, which are expected to favour the occurrence of decarbonation phenomena.

The fact that the original apatite carbonation is lost during SPS represents the weakness point of the proposed process. To the best of our knowledge, only two works focused on the obtainment of nanostructured calcium phosphates succeeded in retaining powders carbonation after SPS **[28-29]**. To achieve this goal, the SPS process was conducted at dwell temperature of 150 °C, i.e., under cold-sintering

conditions, mechanical pressures in the range 80-100 MPa, 10-13 min holding time, and argon environment. However, depending on the starting powders, the relative densities achieved by the resulting products were rather low, i.e. 60% **[28]**, and 62-73 % **[29]**. Therefore, more severe processing conditions are required to improve the densification level.

3.2.2 SEM and TEM analysis

SEM observations (**Figure S13**) confirmed that powder sintering is progressively promoted with the dwell temperature increase. Samples obtained at 750°C by SPS (**Figure S13a**) are poorly consolidated, with a significant residual porosity, in agreement with the corresponding low relative density values (about 60%, cf. **Table 1**). On the other hand, ceramics sintered at higher temperatures, particularly at 900°C (**Figure S13b**), displayed a reasonably good densification level, even though porosity was not eliminated, consistently with the resulting SPS product density (approximately 91%, cf. **Table 1**). A detailed SEM image of the latter sample is shown in **Figure 5a**, indicating that a uniform microstructure with well-defined grains is obtained. Grain size distribution evaluated from SEM micrographs (about 900 measurements) is reported in **Figure 5b.** The resulting mean and median values are 115 ± 42 nm and 108 nm, respectively. Image analysis also provided an estimate of pores size, i.e. 100 ± 40 nm, based on 30 measurements.

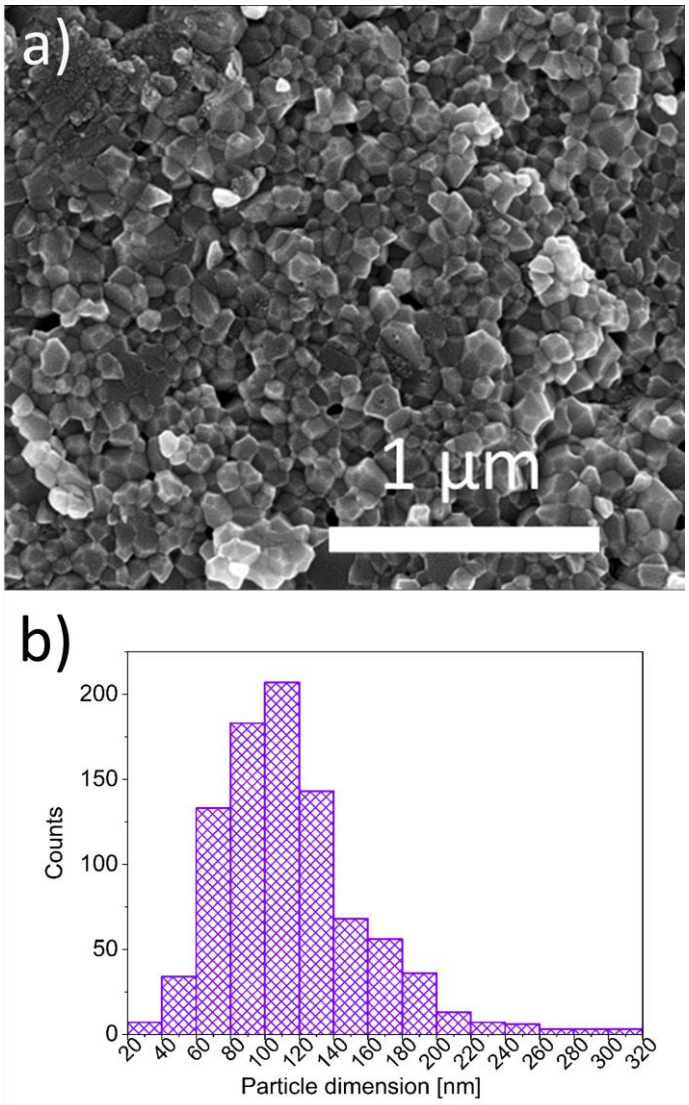

Figure 5. SEM micrograph **(a)** and grain size distribution **(b)** of the sample produced by SPS at 900°C.

Additional data are obtained from HR-TEM analysis (**Figures 6 and S14**). Firstly, it should be noted that the use of low-intensity electron beam was necessary to prevent damage of the examined sample, apparently very sensitive to the electron beam, as evidenced by the spots enclosed in the white circle of the image shown in **Figure S14**. Secondly, as indicated by the dash lines in the same image, the grains dimension, being approximately 100 nm, is in line with the previously reported XRD and SEM analyses. This also holds regarding pore size, on the order of few hundreds of nm (light areas in **Figure 6a**).

Moreover, the SADP measurements resulted in spot-like patterns, as shown in **Figure 6b**. This means that it was not possible to generate a profile, as for the case of powders. Nonetheless, the obtained SADP is clearly due to the polycrystalline nature of the sample. The d-spacing corresponding to diffraction spots were calculated from this pattern; the obtained values are compatible with some of the main apatite planes, namely 8.19 Å (100), 5.29 Å (101), and 3.42 Å (002).

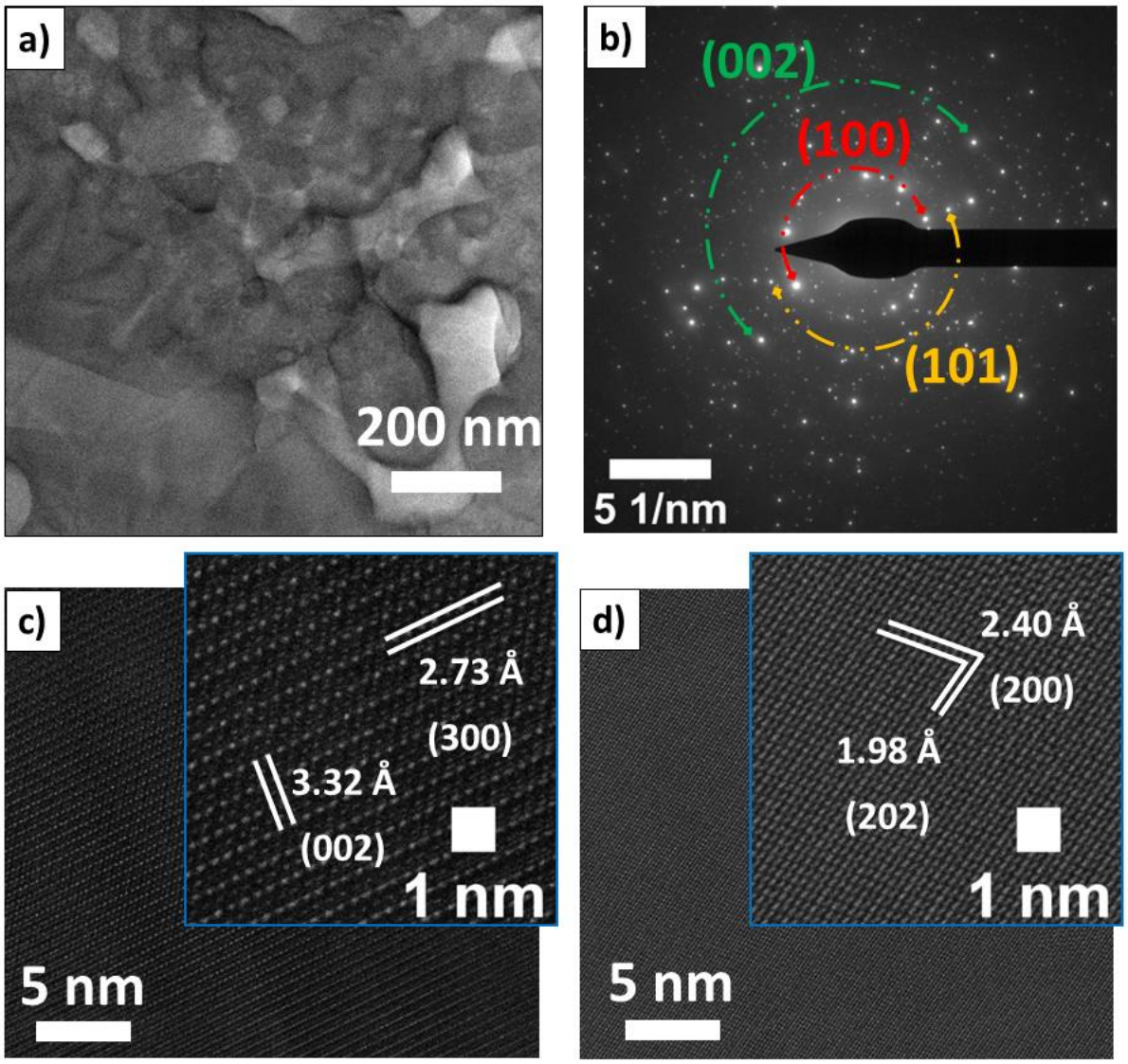

Figure 6. HR-TEM images (a), related SADP (b), low electron dose HRTEM images (c)-(d) acquired from different parts of the sample produced by SPS at 900°C with the corresponding magnifications reporting d-spacing measurements ascribable to apatite (c), and β-TCP (d).

Some examples of d-spacing measurements carried out on low electron dose high-resolution TEM micrographs and ascribed to apatite and β-TCP crystal structures are shown in **Figure 6c** and **Figure 6d**, respectively. Specifically, the measured distances of 3.32 Å and 2.73 Å in **Figure 6c** could be associated with nominal values of HA structure, i.e., 3.42 Å (0, 0, 2) and 2.72 Å (3, 0, 0), respectively. In addition, data obtained from **Figure 6d** (1.98 Å and 2.40 Å) can be ascribed to β-TCP, whose nominal values are 1.99 Å (2, 0, 2) and 2.33 Å (2, 0, 0), respectively.

The presence of both phases was confirmed by the EDS analysis (**Figure S15)**. Indeed, the ratio between Ca and P peaks intensities was found to be 1.66 (**Figure S15a**) and 1.48 (**Figure S15b**), very close to the nominal values for HA (1.67) and β-TCP (1.5).

The latter findings further testify, coherently with previous analyses, that the samples obtained by SPS from combustion synthesized powders consist of these two calcium phosphate phases, being apatite the main one present in the bulk, in coexistence with β-TCP.

Based on the obtained results, it is possible to state that the proposed process allows for the fabrication of about 91 % dense nanostructured apatite-rich composites, with β-TCP as a second phase. Future process improvements include powder sintering conducted in an inert environment instead of vacuum, and the use of higher mechanical loads, taking advantage of suitable high-pressure cells, to reduce the dwell temperature required to achieve adequate densification levels. Indeed, both would allow to avoid, or retain the observed decarbonation of apatite as well as grains growth, so that more suitable bioceramics will be produced. Of course, their final performances must be assessed by the required biological characterization, with specific in-vitro tests (both acellular and cellular). Furthermore, the possibility of incorporating therapeutic ions in calcium phosphate structures during the SCS process (in-situ) will be also considered in future studies.

4 Concluding remarks

In this work, bulk apatite-based bioceramics were produced by SPS of nanoscale powders prepared by the SCS method. The main results are summarized in what follows.

a) The ignition time of the synthesis reaction is minimized when operating under stoichiometric conditions, i.e., the fuel-to-oxidizer ratio was equal to 1, whereas the yield in the apatite phase is maximized with a small excess of fuel (ϕ=1.1).

b) A post-synthesis heat treatment was required to eliminate secondary phases present in the combustion synthesized powders: under the optimal annealing conditions (700°C/3h), the obtained powders consisted of 83 wt.% of apatite, with crystallites size less than 70 nm, 16.7% TCP (13.5 and 3.2% of the β- and α- phases, respectively) and traces of CaO. In addition, the resulting apatite phase possessed a carbonation level of about 2 wt.%.

c) During powders consolidation by SPS, an increase of the temperature from 750 to 900°C led to bulk samples with relative density of about 91% of the theoretical value of HA. Correspondingly, only a minor decomposition of apatite occurred, with the latter (about 78 wt.%) and β-TCP (22 wt.%) the only phases present in the sintered sample.

d) The obtained bioceramic possesses uniform morphology, and maintains the nanoscale structure of the synthesized powders, with apatite grains size growing slightly above 100 nm.

Based on the features above, the nanostructured biphasic product developed in this work is expected to display improved biocompatibility and resorbability compared to conventional microcrystalline hydroxyapatite, which is of fundamental importance in the field of regenerative medicine.

Acknowledgments

Damiano Angioni performed his activity in the framework of the International Ph.D. in Innovation Sciences and Technologies at the University of Cagliari, Italy.

5 References

[1] S.V. Dorozhkin, Calcium orthophosphate bioceramics, Ceram. Int. 41(10) (2015) 13913–13966, https://doi.org/10.1016/j.ceramint.2015.08.004

[2] S.V. Dorozhkin, Multiphasic calcium orthophosphate (CaPO4) bioceramics and their biomedical applications, Ceram. Int. 42(6) (2016) 6529-6554. https://doi.org/10.1016/j.ceramint.2016.01.062

[3] J.-M. Bouler, R.Z. LeGeros, G. Daculsi, Biphasic calcium phosphates: Influence of three synthesis parameters on the HA/β-TCP ratio, J. Biomed. Mater. Res. 51(4) (2000) 680-684. https://doi.org/10.1002/1097-4636(20000915)51:4<680::aid-jbm16>3.0.co;2-%23

[4] E. C. Victoria, F. D. Gnanam, Synthesis and Characterization of Biphasic Calcium Phosphate, Trends Biomater. Artif. Organs 16(1) (2002) 12-14.

[5] A. Eskandari, M. Aminzare, H. Hassani, H. Barounian, S. Hesaraki, S.K. Sadrnezhaad, Densification behavior and mechanical properties of biomimetic apatite nanocrystals, Curr. Nanosci. 7(5) (2011) 776-780. https://doi.org/10.2174/157341311797483646

[6] A.N. Natasha, R. Singh, M. Hamdi, T.C. Young, J. Purbolaksono, I. Sopyan, R. Toulouei, Synthesis and properties of biphasic calcium phosphate prepared by different methods, Adv. Mater. Res. 970 (2014) 20-25. https://doi.org/10.4028/www.scientific.net/AMR.970.20

[7] A. Cuccu, S. Montinaro, R. Orrù, G. Cao, D. Bellucci, A. Sola, V. Cannillo, Consolidation of different hydroxyapatite powders by SPS: Optimization of the

sintering conditions and characterization of the obtained bulk products, Ceram. Int. 41(1), (2015) 725-736. https://doi.org/10.1016/j.ceramint.2014.08.131

[8] P. Nandha Kumar, S.K. Mishra, R. Udhay Kiran, S. Kannan, Preferential occupancy of strontium in the hydroxyapatite lattice in biphasic mixtures formed from non-stoichiometric calcium apatites, Dalton Trans. 44(17) (2015) 8284-8292. https://doi.org/10.1039/c5dt00173k

[9] S. Kannan, J.M.F. Ferreira, Synthesis and thermal stability of hydroxyapatite-β-tricalcium phosphate composites with cosubstituted sodium, magnesium, and fluorine, Chem. Mater. 18(1) (2006) 198-203. https://doi.org/10.1021/cm051966i

[10] T.-W. Kim, H.-S. Lee, D.-H. Kim, H-H. Jin, K-H. Hwang, J. K. Lee, H.-C. Park, S.-Y. Yoon, In situ synthesis of magnesium-substituted biphasic calcium phosphate and in vitro biodegradation, Mater. Res. Bull. 47(9) (2012) 2506-2512, https://doi.org/10.1016/j.materresbull.2012.05.011

[11] M. Ahmadi, G. Dini, M. Afshar, F. Ahmadpour, Synthesis, characterization, and bioactivity evaluation of biphasic calcium phosphate nanopowder containing 5.0 mol% strontium, 0.6 mol% magnesium, and 0.2 mol% silicon for bone regeneration, J. Mater. Res. 37(11) (2022) 1916-1928. https://doi.org/10.1557/s43578-022-00604-3

[12] T. Matić, M.L. Zebić, V. Miletić, I. Cvijović-Alagić, R. Petrović, D. Janaćković, D. Veljović, Sr,Mg co-doping of calcium hydroxyapatite: Hydrothermal synthesis, processing, characterization and possible application as dentin substitutes Ceram. Int. 48(8) (2022) 11155-11165 https://doi.org/10.1016/j.ceramint.2021.12.335

[13] J. Pena, M. Vallet-Regí, Hydroxyapatite, tricalcium phosphate and biphasic materials prepared by a liquid mix technique, J. Eur. Ceram. Soc. 23(10) (2003) 1687-1696. https://doi.org/10.1016/S0955-2219(02)00369-2

[14] A. Farzadi, M. Solati-Hashjin, F. Bakhshi, A. Aminian, Synthesis and characterization of hydroxyapatite/β-tricalcium phosphate nanocomposites using microwave irradiation, Ceram. Int. 37(1) (2011) 65-71. https://doi.org/10.1016/j.ceramint.2010.08.021

[15] J. Chen, Y. Wang, X. Chen, L. Ren, C. Lai, W. He, Q. Zhang, A simple sol-gel technique for synthesis of nanostructured hydroxyapatite, tricalcium phosphate and biphasic powders, Mater. Lett. 65(12) (2011) 1923-1926. https://doi.org/10.1016/j.matlet.2011.03.076

[16] M. Ebrahimi, M. Botelho, W. Lu, N. Monmaturapoj, Synthesis and characterization of biomimetic bioceramic nanoparticles with optimized physicochemical properties for bone tissue engineering, J. Biomed. Mater. Res. A 107(8) (2019) 1654-1666. https://doi.org/10.1002/jbm.a.36681

[17] S.K. Ghosh, S.K. Nandi, B. Kundu, S. Datta, D.K. De, S.K. Roy, D. Basu, In vivo response of porous hydroxyapatite and β-tricalcium phosphate prepared by aqueous solution combustion method and comparison with bioglass scaffolds J. Biomed. Mater. Res. B 86(1) (2008) 217-227. https://doi.org/10.1002/jbm.b.31009

[18] R. Ramakrishnan, P. Wilson, T. Sivakumar, I. Jemina, A comparative study of hydroxyapatites synthesized using various fuels through aqueous and alcohol mediated combustion routes, Ceram. Int. 39(4) (2013) 3519-3532. https://doi.org/10.1016/j.ceramint.2012.10.176

[19] A. Varma, A.S. Mukasyan, A.S. Rogachev, K.V. Manukyan, Solution Combustion Synthesis of Nanoscale Materials, Chem. Rev. 116(23) (2016) 14493–14586. https://doi.org/10.1021/acs.chemrev.6b00279

[20] S.T. Aruna, M. Shilpa, Solution combustion synthesis of calcium phosphate-based bioceramic powders for biomedical applications, Springer Series in

Biomaterials Science and Engineering 16 (2021) 175-196. https://doi.org/10.1007/978-981-33-6252-9_7

[21] S.V. Dorozhkin, Nanodimensional and nanocrystalline apatites and other calcium orthophosphates in biomedical engineering, biology and medicine, Materials 2(4), 2009 pp. 1975-2045 https://doi.org/10.3390/ma2041975

[22] M. Canillas, R. Rivero, R. García-Carrodeguas, F. Barba, M.A. Rodríguez, Processing of hydroxyapatite obtained by combustion synthesis, Bol. Soc. Esp. Ceram. Vidr. 56(5) (2017) 237–242. https://doi.org/10.1016/j.bsecv.2017.05.002

[23] R. Ghosh, R. Sarkar, Synthesis and characterization of sintered hydroxyapatite: a comparative study on the effect of preparation route, J. Aust. Ceram. Soc. 54(1) (2018) 71-80. https://doi.org/10.1007/s41779-017-0128-5

[24] K.A. Khor, R. Kumar, P Cheang, Process-phase-properties relationship in radio frequency (RF) plasma synthesized hydroxyapatite (HA), Surf. Coat. Technol. 177-178 (2004) 740-746. https://doi.org/10.1016/j.surfcoat.2003.08.015

[25] X. Guo, J.E. Gough, P. Xiao, J. Liu, Z. Shen, Fabrication of nanostructured hydroxyapatite and analysis of human osteoblastic cellular response. J. Biomed. Mater. Res. A 82A (2007) 1022–1032. https://doi.org/10.1002/jbm.a.31200

[26] F. Zhang, K. Lin, J. Chang, J. Lu, C. Ning, Spark plasma sintering of macroporous calcium phosphate scaffolds from nanocrystalline powders. J. Eur. Ceram. Soc. 28 (2008) 539–545. https://doi.org/10.1016/j.jeurceramsoc.2007.07.012

[27] C. Drouet, F. Bosc, M. Banu, C. Largeot, C. Combes, G. Dechambre, C. Estournes, G. Raimbeaux, C. Rey, Nanocrystalline apatites: From powders to biomaterials. Powder Technol. 190 (2009) 118–122. https://doi.org/10.1016/j.powtec.2008.04.041

[28] M. Luginina, R. Orrù, G. Cao, D. Grossin, F Brouillet, G Chevallier, C. Thouron, C. Drouet, First successful stabilization of consolidated amorphous calcium

phosphate (ACP) by cold sintering: Toward highly-resorbable reactive bioceramics, J. Mater. Chem. B 8(4) (2020) 629-635. https://doi.org/10.1039/c9tb02121c

[29] C. Ortali, I. Julien, C. Drouet, E. Champion, Influence of carbonation on the low-temperature consolidation by Spark Plasma Sintering of carbonated calcium phosphate bioceramics, Ceram. Int. 46(5) (2020) 5799-5810. https://doi.org/10.1016/j.ceramint.2019.11.030

[30] X. Guo, P. Xiao, J. Liu, Z. Shen, Fabrication of nanostructured hydroxyapatite via hydrothermal synthesis and spark plasma sintering, J. Am. Ceram. Soc. 88 (2004) 1026–1029. https://doi.org/10.1111/j.1551-2916.2005.00198.x

[31] M. Eriksson, Y. Liu, J. Hu, L. Gao, M. Nygren, Z. Shen, Transparent hydroxyapatite ceramics with nanograin structure prepared by high pressure spark plasma sintering at the minimized sintering temperature, J. Eur. Ceram. Soc. 31(9) (2011) 1533-1540. https://doi.org/10.1016/j.jeurceramsoc.2011.03.021

[32] S. K. Ghosh, S.K. Roy, B. Kundu, S. Datta, D. Basu, Synthesis of nano-sized hydroxyapatite powders through solution combustion route under different reaction conditions, Mater. Sci. Eng. B 176 (2011) 14-21. https://doi.org/10.1016/j.mseb.2010.08.006

[33] L. Lutterotti, R. Ceccato, R. Dal Maschio, E. Pagani, Quantitative analysis of silicate glass in ceramic materials by the Rietveld method. Mater. Sci. Forum, 87 (1998) 278-281. https://doi.org/10.4028/www.scientific.net/MSF.278-281.87

[34] C. A Schneider, W. S. Rasband, K. W Eliceiri, NIH Image to ImageJ: 25 years of image analysis, Nat. Methods 9(7) (2012), 671-675. https://doi.org/10.1038/nmeth.2089

[35] J.L. Lábár, Consistent indexing of a (set of) SAED pattern(s) with the ProcessDiffraction program, Ultramicroscopy 103 (2005) 237-249. https://doi.org/10.1016/j.ultramic.2004.12.004

[36] P. Sapkota, A. Aprahamian, K.Y. Chan, B. Frentz, K. T. Macon, S. Ptasinska, D. Robertson, K. Manukyan, Irradiation-induced reactions at the $CeO_2/SiO_2/Si$ interface, J. Chem. Phys. 152(10) (2020) 104704. https://doi.org/10.1063/1.5142619

[37] K. Momma and F. Izumi, VESTA: a three-dimensional visualization system for electronic and structural analysis, J. Appl. Crystallogr. 41 (2008) 653-658. https://doi.org/10.1107/S0021889808012016

[38] M.E. Fleet, Carbonated hydroxyapatite: materials, synthesis, and applications, Jenny Stanford Publishing, 2015, pp. 55-96

[39] K.S.P. Karunadasa, C.H. Manoratne, H.M.T.G.A. Pitawala, R.M.G. Rajapakse, Thermal decomposition of calcium carbonate (calcite polymorph) as examined by in-situ high-temperature X-ray powder diffraction, J. Phys. Chem. Solids 134 (2019) 21-28. https://doi.org/10.1016/j.jpcs.2019.05.023

[40] A. Awonusi, M.D. Morris, M.M.J. Tecklenburg, Carbonate assignment and calibration in the Raman spectrum of apatite, Calcif. Tissue Int. 81(1) (2007) 46–52. https://doi.org/10.1007/s00223-007-9034-0